applied optics

Imaging and emission spectroscopy of the submicrosecond plasma generated from copper substrate with nanosecond laser pulses

Mateusz Tanski,[1,*] Robert Barbucha,[1] Jerzy Mizeraczyk,[2] and Szymon Tofil[3]

[1]Institute of Fluid Flow Machinery, Polish Academy of Sciences, Gdansk, Poland
[2]Department of Marine Electronics, Gdynia Maritime University, Gdynia, Poland
[3]Faculty of Mechatronics and Mechanical Engineering, Kielce University of Technology, Kielce, Poland
*Corresponding author: tanski@imp.gda.pl

Received 18 June 2020; revised 19 August 2020; accepted 21 August 2020; posted 21 August 2020 (Doc. ID 400488); published 17 September 2020

In this paper, an experimental investigation of the ablation plasma generated from the copper substrate by means of nanosecond laser pulses is presented. We studied the evolution of the ablation plasma in the first 1000 ns after plasma onset using the fast-gated imaging and optical emission spectroscopy methods. Plasma imaging showed that the expansion of the plume front can be described using a so-called drag model, with the expansion limit increasing with laser fluence from 254 μm for 30 J/cm^2 to 375 μm for 67 J/cm^2. By using the Boltzmann plot and Stark broadening methods, it was found that within the first microsecond after onset, the electron excitation temperature and electron number density decrease from 1.2 eV to 0.8 eV and from 4×10^{16} cm^{-3} to 5×10^{15} cm^{-3}, respectively. Using the McWhirter criterion, we confirmed that in the considered time range the plasma remains in a state of local thermodynamic equilibrium.

https://doi.org/10.1364/AO.400488

1. INTRODUCTION

Since the invention of the laser in 1962, particularly great scientific interest has concerned the investigation of ablation plasmas (generated with laser radiation) at a relatively late stage of the plasma lifetime. This is somehow justified by the practical interest in the development of the laser-induced breakdown spectroscopy (LIBS) technique [1–5], for which the analysis of the radiation emitted by the plasma is typically performed at times longer than 1000 ns after the onset of the plasma. In comparison, the properties of ablation plasmas at the earlier stages of their evolution (in the nanosecond time range) have been investigated superficially, and only a limited number of studies have focused on this subject. However, a better understanding of the early stage of plasmas is beneficial for applications such as laser micro- and nanomachining, plasma sputtering deposition, synthesis of nanoparticles, laser-assisted material analysis, laser ion sources, and others.

Recently, Wu *et al.* [6] studied the early stage of a tungsten plasma (up to 1000 ns after plasma onset) generated with nanosecond laser pulses in air at a pressure of 10 mbar. The time-resolved images showed that under reduced pressure, the plasma expanded hemispherically for only up to 100 ns after the laser pulse, and afterwards the plasma took a plume-like shape. Hermann *et al.* [7] investigated plasma produced via laser ablation of a steel sample with 4 ns laser pulses. They found that the kinetic pressure within the ablated plume decreased monotonically with elapsing time for up to a few microseconds after plasma onset. Freeman *et al.* [8] reported on the physics of copper plasma (up to 2000 ns after the plasma onset) generated using 8 ns and 40 fs laser pulses in a vacuum and air. He found that the presence of the air enhanced the plasma density and temperature by limiting the process of plasma expansion. Qiu *et al.* [9] studied the plasma dynamics expanding in ambient air using a fast-gated imagining technique. In his research, he used 1064 nm, 8 ns laser pulses focused onto a brass target. He observed that the shock wave generated during laser ablation of the target material detached from the plasma front at a very early stage, and both traveled separately at different velocities.

Elnasharty [10] studied the influence of laser pulse parameters (energy and duration) on the spectroscopic properties of the early stage plasma generated from an aluminum target. He found that both the electron number density and ionization temperature increase with increasing laser fluence and decreasing pulse duration. Similar results were reported by Rahman *et al.* [11] who studied the spectroscopic properties of plasma generated during laser ablation of a glass substrate. Unnikrishnan *et al.* [12] investigated copper plasma generated by means of 6 ns laser pulses using the optical emission spectroscopy method in the time range from 300 ns up to 2000 ns

after plasma onset. They concluded that the considered plasma was in local thermodynamic equilibrium (LTE) only in a short time window between 700 ns and 1000 ns after plasma onset. Skocic *et al.* [13] reported on the formation of the double layer in an early stage copper plasma generated using nanosecond laser pulses in ambient argon under reduced pressure. Using an optical time-of-flight method, he found that three consecutive beams were emitted from the irradiated zone. The first was associated with Cu III ions followed by Cu II ions and finally by a beam of neutral Cu I atoms.

In this paper, we report on the experimental studies of laser-induced ablation plasma generated in ambient air from the surface of a copper target irradiated by nanosecond laser pulses. We studied the formation and expansion of the plasma plume at the early stage of its evolution (up to 1000 ns after plasma onset) using the optical imaging and emission spectroscopy methods. Optical imaging of the early stage plasma revealed that the plume front expansion can be described using the so-called drag model, and the plume expansion limit increases with the laser fluence. By applying the spectroscopic methods of a Boltzmann plot and Stark broadening, we found the temporal variation of the electron excitation temperature and the electron density in the plasma plume.

2. EXPERIMENTAL

In order to examine ablation plasma at its early stage, we used the fast-gated optical imaging and emission spectroscopy techniques. In both of these techniques, a train of laser pulses was used to induce a series of quasi-identical plasmas from the target surface. Each image and spectrogram in the series corresponding to succeeding pulses was delayed by the constant interval of Δt with respect to the previous one. As a result, a set of time-resolved images and spectrograms of the plasma was recorded, each representing the plasma at a different point in time of its evolution.

A. Laser Setup

The laser used for plasma generation (Fig. 1) was a multimode neodymium-doped yttrium aluminum garnet (Nd:YAG) (Quantel Big Sky Laser) solid state laser with second harmonic generation ($\lambda = 532$ nm). The laser pulse power shape was monitored with a Thorlabs DET10A fast photodiode and displayed on an oscilloscope. The pulse width measured at FWHM was 26 ns $\pm$ 1 ns, and the pulse-to-pulse energy stability was 2%.

The ablation plasma was generated by focusing the laser pulses onto the surface of a copper target using a 100 mm focal lens (diameter of the laser spot on the target surface was 60 μm). The target was a 500-μm-thick plate made of 110-type copper alloy (99.9% Cu). After each pulse, the copper target was shifted stepwise horizontally, so that the next pulse hit the target in a previously non-irradiated spot. The laser fluence on the target surface was a variable parameter ranging from 30 J/cm^2 to 67 J/cm^2, varied by altering the peak power energy (the duration and general shape of the laser pulse were not affected when changing its peak power). The ablation plasma was induced in ambient air under atmospheric pressure and a temperature of 23°C.

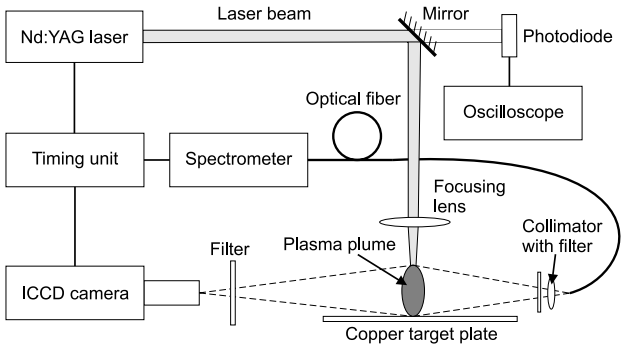

Fig. 1. Experimental setup for investigation of laser ablation plasma using imaging and optical emission spectroscopy methods.

B. Plasma Imaging Setup

The imaging of the ablation plasma was performed using an Andor iStart fast-gated intensified CCD (ICCD) camera with a resolution of 1024 × 1024 pixels. The ICCD camera was equipped with 10 times magnification Nikon microscopic lens, and an NF533-17 bandpass optical notch filter ($\lambda = 533$ nm) was used to suppress the scattered laser radiation (and protect the camera from damage). The ICCD camera was focused onto the region of plasma formation (field of observation size was 550 μm × 550 μm). The time delay between the laser pulse and ICCD camera trigger was set using a Tektronix AFG3102 delay generator. The ICCD images of the plasma plume were captured at times ranging from −33 ns to 60 ns, where $t = 0$ corresponds to the peak of the laser pulse power. The temporal resolution of the recorded set of plasma images was $\Delta t = 1$ ns, and the ICCD camera gating time was $\Delta t = 2$ ns. The plasma plume imaging was carried out for three values of the laser pulse fluence $F_1 = 30$ J/cm^2, $F_2 = 45$ J/cm^2, and $F_3 = 67$ J/cm^2.

C. Plasma Spectroscopy Setup

The emission spectra of the plasma radiation were registered with an Andor Mechelle 500 fiber-coupled, echelle-type spectrometer with an Andor iStar ICCD camera. The gratings of the spectrometer were 52 groves/mm, resulting in a spectral range from 250 nm to 850 nm and a resolution of about 0.05 nm. The plasma radiation was focused onto the entrance of the optical fiber using a single lens collimator placed at a fixed distance of 100 mm from the plasma plume, at angle of 45° to the target surface. Thus, the spectrometer registered the average radiation (spatially integrated) emitted from the entire plasma region. In order to suppress any scattered laser radiation, optical filters were mounted in front of the collimator. Since we were not able to find an optical notch filter suitable for the full spectral range of the spectrometer, we used two filters interchangeably: a 495SOSP filter from Omega Optical [transparent for UV and near-visible (VIS) radiation ranging from 250 nm to 500 nm] and a NF533-17 filter from Thorlabs (transparent for VIS radiation ranging from 400 nm to 850 nm, except a narrow band around $\lambda = 532$ nm). For each time delay Δt, the plasma

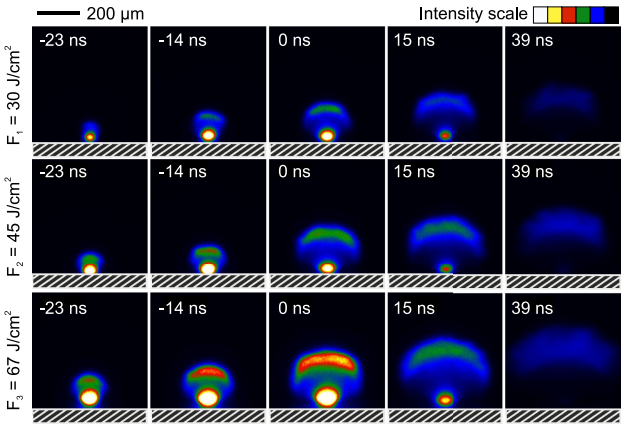

Fig. 2. Evolution of laser-generated plasma in ambient air at early stage of expansion for various laser fluences. Laser pulse width, 26 ns; ICCD camera exposure time, 2 ns.

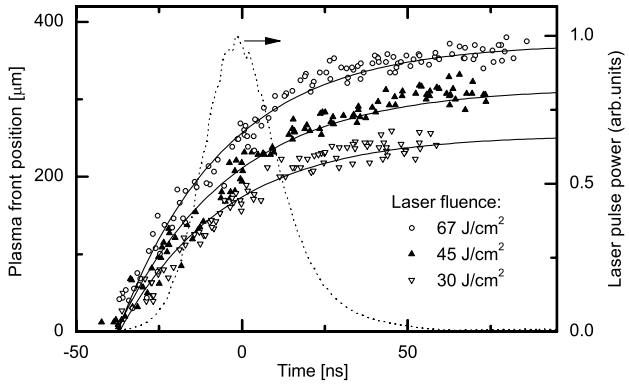

Fig. 3. Plasma plume front position for three values of laser fluence. Data points are fitted with drag model curves (solid lines). Dotted line represents the normalized power of the laser pulse (right-side vertical axis) as a function of time.

spectrum was recorded twice: with the UV-transparent filter and with the VIS-transparent filter. Next, both spectra were combined during data processing, resulting in a full range spectrum. The plasma emission spectra were recorded on time delays, ranging from $t = -50$ ns to $t = 1040$ ns, with a temporal resolution of $\Delta t = 10$ ns and a gating time of 2 ns. The laser fluence was a constant parameter $F = 45\ J/cm^2$.

3. RESULT AND DISCUSSION

A. Imaging of Plasma Plume

The process of plume formation and expansion can be followed by viewing the consecutive series of time-resolved images shown in Fig. 2. In each image, the copper target is located at the bottom and marked with a hashed area, and the laser beam is directed from the top, perpendicular to the target surface. The different colors represent the relative intensity of the emitted radiation (black, minimal; white, maximal). The time delay Δt of each image (in relation to the laser pulse peak) is marked in its corner.

As can be seen in Fig. 2, the plasma expansion process looks similar regardless of the laser fluence. The plasma appears at the time $t = -30$ ns (i.e., 30 ns before the pulse peak) and expands into a form that resembles a mushroom-like shape. After $t = 40$ ns, the plasma starts to decay. It was possible to monitor the plasma decay process until the intensity of the emitted radiation decreased below the sensitivity threshold of the ICCD camera, i.e., to time $t = 60$ ns. It can be seen that the intensity of the plasma radiation increases with the laser fluence. This can be explained by the fact that an increase in the laser fluence enhances the number density of electrons and species in the plume, which is, alongside the excitation temperature, the main factor affecting the total emission intensity [14–16].

The particles ejected from the irradiated region of the target material leave a layer of phase discontinuity (the Knudsen layer) with the majority of the particles having their velocity vector in the direction perpendicular to the target surface [17,18]. In the initial stage of the plasma formation, the particles emitted by the leading edge of the laser pulse form a small but dense plasma spot over the material surface, and, since the ablation continues over the whole pulse duration, this near-surface plasma is sustained by the newly ejected particles. The energetic particles of the expanding, early plasma collide with molecules of the ambient air, which leads to their deceleration and formation of a traveling plasma front on the plasma-air boundary. On the other hand, the plasma particles produced by the later part of the laser pulse, which travel behind the plasma front, do not experience deceleration from the ambient air, as they travel in the channel developed by the preceding particles until they catch up with the plasma front. Thus, the region between the surface plasma and plasma front is characterized by a relatively low density, and no significant emission is recorded from this region. Using the time-resolved images of the plasma plume, we determined the transient position of the plasma front as a function of time (Fig. 3).

The position of the plasma front expanding in the ambient gas can be described mainly by two alternative models: (i) blast wave model and (ii) drag model. The blast wave model assumes that the plasma front follows very closely to the blast wave (generated during laser ablation of the material) described by the classic Sedov–Taylor theory [19,20]. In this model, the plasma initially expands at supersonic velocity, but is gradually decelerated until its velocity reaches the speed of sound. In contrast, in the drag model, the initial high expansion velocity of the plasma front is continuously decelerated by the ambient gas molecules until the plasma front reaches its expansion limit (called the stopping distance) [21]. As seen in the Fig. 3, the plasma front initially (for times $t = 30$ ns) propagates at a relatively high velocity (of an order of 10^3 m/s), but is constantly decelerated with elapsing time, until its velocity decreases below the speed of sound (to about 100 m/s for $t = 360$ ns). As a result of this deceleration, the plasma front approaches its expansion limit. This suggests that the drag model better describes the expansion of the plasma front in the discussed case than the blast wave model, in which the velocity of the plasma front would decrease only to the speed of sound and continue its expansion. Assuming the drag model, the plasma front position R_s in time is described by Eq. (1):

$$R_S = R_{\max}(1 - e^{-\beta t}), \tag{1}$$

where R_{max} is the expansion limit of the plume, and β is the slowing coefficient. The experimental points in Fig. 3 were approximated with curves described by Eq. (1). Based on the approximation parameters, it was found that the expansion limit R_{max} of the plume increases with the laser fluence ($R_{max} = 254\ \mu m$ for $F_1 = 30\ J/cm^2$, $R_{max} = 312\ \mu m$ for $F_2 = 45\ J/cm^2$, and $R_{max} = 372\ \mu m$ for $F_3 = 67\ J/cm^2$). However, the slowing coefficient was found to be independent on the laser fluence $\beta = 3.15 \times 10^{-11}\ s^{-1} \pm 0.3 \times 10^{-11}\ s^{-1}$. The average velocity of the plasma plume front in the first 100 ns after the onset ranges from 2.4×10^3 m/s to 3.6×10^3 m/s and increases with the laser fluence. It is interesting to compare the obtained results with the work done by Zhou *et al.* [22], who investigated a plasma plume generated from a silicon target in ambient air using laser pulses of similar parameters ($\lambda = 1064$ nm, $t = 200$ ns, $F = 40\ J/cm^2$) to those used in our study. They suggested that the expansion of the plasma front generated by the nanosecond laser pulses in ambient air can be reasonably well described by the blast wave model. However, the results of our studies did not confirm this thesis, but rather support drag model expansion. This inconsistency of conclusions may be due to fact that Zhou in his work observed the plasma plume only up to 400 ns after onset, in which the plasma front was still expanding with supersonic velocity, which might wrongly suggest the blast wave model of plasma expansion.

B. Plasma Spectroscopy

Typical examples showing the temporal evolution of the emission spectrum of the laser ablation plasma (for three time delays: 0 ns, 90 ns, 450 ns) are given in Fig. 4. It is worth noting that the lack of a spectrum signal around the 532 nm band is the result of the use of the optical filter matched to the laser wavelength. From Fig. 4, we can observe that the plasma spectrum at the early stage of plume formation (for $t = 0$ ns) is characterized by a relatively large amount of continuum radiation. Generally, there are two main phenomena occurring in the plasma plume that are responsible for the emission of continuum radiation: (i) the radiative two-body recombination of ionized species (effect of the free–bound transitions) and (ii) bremsstrahlung (effect of the free–free transitions) [23]. In the early stage plasma, the contribution of the bremsstrahlung process to the emission of continuum radiation prevails over the radiative recombination, since, at this stage, the plasma recombines mainly via non-radiative three-body processes [24,25]. Apart from the continuum radiation in the early stage spectrum ($t = 0$), we also observe a wideband emission component of the 377.06 nm line and the doublet 435.26 nm and 437.65 nm (FWHM of those lines is about 25 nm) attributed to the electronic transitions within excited copper ions (Cu III). The broadening of those Cu III spectral lines is a result of the Stark effect, which is caused by the electric field within the dense plasma at the early stage of its evolution. Such wide line bands corresponding to the highly ionized ions at the early stage of the plasma expansion were also reported in Refs. [8,26,27]. As the plasma density decreases with elapsing time, the Stark broadening effect becomes weaker and ionic Cu II lines appear in the plasma spectrum (for $t = 90$ ns), followed by atomic spectral lines Cu I (for $t = 450$ ns). This time sequence of species appearance in the plume is the result of

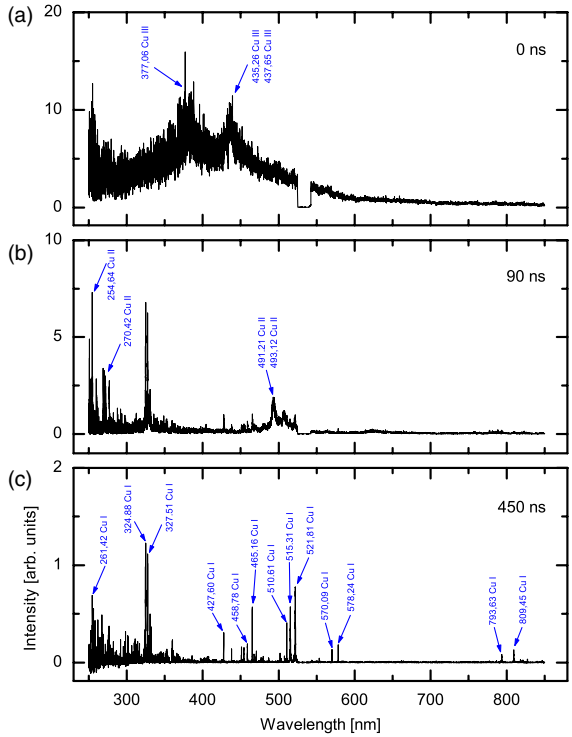

Fig. 4. Typical examples of the plasma spectrum generated from the copper target. The measurements were taken at time delays: (a) 0 ns, (b) 90 ns, and (c) 450 ns, with respect to the laser pulse maximum ($t = 0$). Laser pulse duration $t_i = 26$ ns and fluence $F = 45\ J/cm^2$. Spectrometer gating time was 2 ns.

the consecutive recombination of the highly ionized Cu III ions to the ions of the lower ionization degree Cu II and eventually to the neutral Cu I atoms.

It is generally accepted that an ablation plasma generated using nanosecond laser pulses can be considered to be a plasma in LTE [28,29], which we confirmed in the latter part of this section using the McWhirter criterion. Accepting this assumption allowed us to apply two methods in order to study the plasma's parameters: (i) a Boltzmann plot analysis to measure the electron excitation temperature and (ii) a Stark spectral line broadening method to determine the electron number density in the plume. For a plasma in LTE, the electron excitation temperature T_{exc}, which describes the population of excited energy atomic levels, and the observed light intensity I_{ki} of radiative transition between levels k and i are related by Eq. (2):

$$\ln\left(\frac{I_{ki}\lambda}{g_k A_{ki}}\right) = -\frac{1}{k_B T_{exc}} E_k + \left(\frac{hcLn}{4\pi P}\right), \tag{2}$$

where λ_{ki} is the transition line wavelength, g_k is the degeneracy of the upper energy level, A_{ki} is the transition probability, k_B is the Boltzmann constant, E_k is the energy of the upper level, L is the characteristic plasma length, n is the number density, and P is the partition function. If, for a given spectrum, we plot the $\ln(I_{ki}\lambda_{ki}/g_k A_{ki})$ component of the selected spectral lines versus the energy E_k, the Boltzmann plot analysis allows us to calculate the electron excitation temperature T_{exc} from the slope of the linear function that approximates the data points. A detailed description of the Boltzmann plot analysis method

Table 1. Spectroscopic Parameters of the Selected Lines of Cu I used for the Boltzmann Plot Analysis

Wavelength λ_{ki} (nm)	Radiative Transition	Upper Level Energy E_k (eV)	$g_k A_{ki}$ (s^{-1})
27.6	$4s5s^4D_{7/2} \rightarrow 4s4p^4P_{5/2}$	7.73	2.76×10^8
458.7	$4s5s\,^4D_{5/2} \rightarrow 4s4p\,^4F_{7/2}$	7.8	1.92×10^8
465.16	$4s5s\,^4D_{7/2} \rightarrow 4s4p\,^4F_{9/2}$	7.73	3.04×10^8
510.61	$4p\,^2P_{3/2} \rightarrow 4s^{22}D_{5/2}$	3.82	8×10^6
515.31	$4\,d\,^2D_{3/2} \rightarrow 4p^2P_{1/2}$	6.19	2.4×10^8
521.81	$4\,d\,^2D_{5/2} \rightarrow 4p^2P_{3/2}$	6.19	4.5×10^8
570.09	$4p\,^2P_{3/2} \rightarrow 4s^{22}D_{3/2}$	3.82	9.6×10^5
578.24	$4p\,^2P_{1/2} \rightarrow 4s^{22}D_{3/2}$	3.79	3.3×10^6

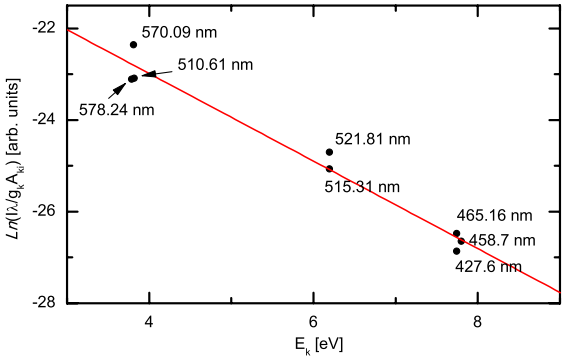

Fig. 5. Boltzmann plot for eight Cu I transition lines corresponding to the spectrum captured at time delay $t = 450$ ns. Solid line, approximation function. Electron excitation temperature $T_{exc} = 1.04 \pm 0.08$ eV.

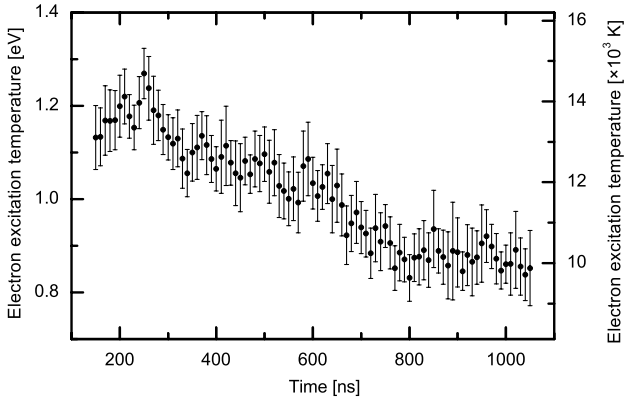

Fig. 6. Temporal variation of the electron excitation temperature in the plasma plume calculated using the Boltzmann plot method.

can be found in Refs. [24,30,31]. In this paper, the electron excitation temperature was determined using the Boltzmann plot method based on the eight preselected Cu I transition lines (Table 1). It should be mentioned here that except from the measuring uncertainty of the lines' intensities, the accuracy of the Boltzmann plot method can be affected by the uncertainty of the transition probabilities, self-absorption of emission lines, as well as a deviation from LTE conditions [27].

A typical Boltzmann plot corresponding to the plasma spectrum captured at time delay $t = 450$ ns is shown in Fig. 5. The data points were reasonably well approximated with a straight line with a coefficient of determination $R^2 = 0.96$. From the slope of the approximation function ($a = -0.96 \pm 0.07$), the electron excitation temperature was calculated to be $T_{exc} = 1.04 \pm 0.08$ eV (12, 070 ± 928 K).

By applying the Boltzmann plot method for all plasma spectra captured at time delays ranging from $t = 150$ ns to $t = 1050$ ns, we found the temporal variation of the electron excitation temperature in the plasma plume (Fig. 6). For the time range considered in Fig. 6, the electron excitation temperature decreases from about 1.12 eV at $t = 150$ ns to about 0.88 eV at $t = 1050$ ns. The Boltzmann plot method could not be successfully applied for spectra captured at times before $t = 150$ ns, since the strong continuum radiation prevents us from accurately determining the intensity of all considered transition lines.

In the regime of nanosecond laser pulses, photothermal ablation of the target material is the main process resulting in the generation of the excited species forming the plasma plume [20]. However, the excitation of the plasma species can also take place afterwards as a result of a plasma shielding process, in which a trailing part of the laser pulse is absorbed by the plasma via photo-excitation [32,33]. Yet, in our studies, the laser pulse ends at about time $t = 50$ ns, so the plasma shielding process after this time is negligible (for the time range from 150 ns to 1050 ns). On the other hand, excitation and de-excitation of the plasma species can also occur due to collisional interactions of the plasma species with each other and with air molecules [34–36]. Since the contribution of the collisional interaction increases with the plasma density, this process results in significant excitation/de-excitation only in the highly dense regions of the near-surface plasma and in the plasma front. As it was shown in Section 3.A, the near-surface plasma disappears with the end of the laser pulse, and the plume expands only up to about 100 ns after the laser pulse, reaching its expansion limit in this time. Thus, it can be assumed that for the time range considered in Fig. 6, neither plasma shielding nor collisional excitation/de-excitation of the plasma species is quantitatively significant. The decrease in the electron excitation temperature can be attributed primarily to the radiative de-excitation of the neutral atoms.

In order to determine the variation of the electron number density in the plasma plume, we applied the Stark broadening method to the 521.81 nm Cu I spectral line. Although the three major mechanisms responsible for the broadening of the spectral lines in the investigated plasma are Doppler broadening, resonance broadening, and Stark broadening, the Doppler and resonance broadenings are much weaker in comparison to the

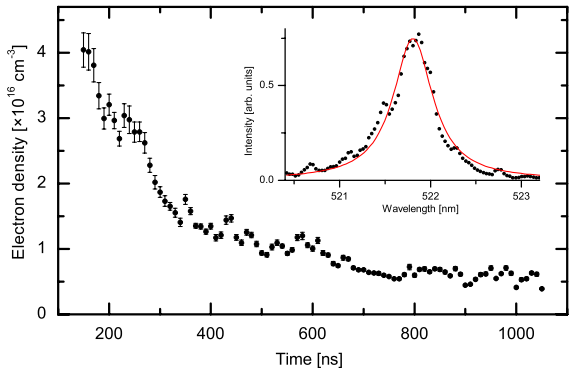

Fig. 7. Temporal variation of the electron number density calculated from the Stark broadening of the Cu I 521.81 nm spectral line. Inserted plot: profile of the Cu I 521.81 nm line captured at time delay $t = 450$ ns, approximated by the Lorentz function (solid red line).

Stark effect and can be neglected in further analyses [37–40]. Spectral lines broadened solely due to the Stark effect have a Lorentzian profile, and, in the first approximation, the FWHM of this profile is given by Eq. (3) [40–44]:

$$\Delta\lambda_{\mathrm{FHWHM}} = 2\omega\left(\frac{n_e}{10^{16}}\right), \tag{3}$$

where ω is the electron impact parameter, and n_e is the electron density. In the following calculations, we took the parameter $\omega = 0.22$ nm (given for a temperature of 10^4 K) from the spectroscopy data tables provided by Konjevic and Wiese [45]. A typical profile of the Cu I 521.81 nm spectral line captured at time delay $t = 450$ ns is shown in the inserted plot in Fig. 7. The line width in this case is $\Delta\lambda_{\mathrm{FWHM}} = 0.571$ nm, which gives an electron number density of $n_e = 1.18 \times 10^{16}\ \mathrm{cm}^{-3}$. Using this method for each spectrum captured in the time range from $t = 150$ ns to $t = 1050$ ns provided the temporal variation of the electron number density in the plasma plume shown in Fig. 7. The electron number density in the plasma plume is equal to $4 \times 10^{16}\ \mathrm{cm}^{-3}$ at time $t = 150$ ns, and, within 1 μs, it decreases almost one order of magnitude to $5 \times 10^{15}\ \mathrm{cm}^{-3}$. We can distinguish two effects responsible for the decreasing of the electron number density in the plasma: plasma expansion, which effectively leads to the dilution of the electrons in the plume, and plasma recombination via inelastic collisions between free electrons and ions. As discussed above, for the time range considered in Fig. 7, the plasma plume had already reached its expansion limit, and the decrease in the electron number density can be attributed mainly to the recombination process.

In order to verify the LTE assumption of the investigated plasma, we applied the McWhirter criterion, which describes the minimal electron number density necessary for collisional sustainment of LTE in the plume [46–48]. The McWhirter criterion is satisfied when the electron number density (expressed in cm^{-3} units) is greater than Eq. (4):

$$n_e \geq 1.6 \cdot 10^{12}\, T_e^{1/2} (\Delta E)^3, \tag{4}$$

where T_e is the electron temperature [in kelvin (K)], and ΔE is the highest energy of the considered radiative transitions [in electron volts (eV)]. In the present study, the highest value of T_e was 1.5×10^4 K (for $t = 250$ ns) and $\Delta E = 2.9$ eV for the transition at 427.6 nm. For those values, the McWhirter criterion is satisfied when $n_e \geq 4.8 \times 10^{15}\ \mathrm{cm}^{-3}$. Figure 7 shows that for the investigated time range (from 150 ns to 1050 ns), the electron number density in the plasma is greater than $5 \times 10^{15}\ \mathrm{cm}^{-3}$, which satisfies the McWhirter criterion and confirms the LTE assumption taken for the calculation of the electron excitation temperature using the Boltzmann plot method and the electron number density using the Stark broadening method.

4. CONCLUSIONS

In this work, we studied ablation plasma generated from a copper target by means of nanosecond laser pulses using the fast-gated imaging and spectroscopy methods. Our studies were focused on the early stage plasma expanding in ambient air up to 1000 ns after plasma onset. Optical imaging revealed that the expansion of the plasma front is decelerated by the air molecules, and, hence, the plasma expands for only up to about 100 ns after the laser pulse, reaching its expansion limit in this time. It was found that the plasma expansion limit increases with the laser fluence. The results suggest that the expansion of a plasma plume in ambient air can be successfully described using the so-called drag model of expansion. Optical emission spectroscopy showed that both the electron excitation temperature and the electron number density decrease in the time range from 150 ns to 1000 ns after the pulse. Since the laser pulse has already ended in this time range, and the plasma has already reached its expansion limit, neither the plasma shielding process nor collisional de-excitation is quantitatively significant, thus the decrease in the electron excitation temperature was attributed primarily to the radiative de-excitation of the neutral atoms in the plasma plume. The decrease in the electron number density is mainly due to the recombination processes taking place in the plume. Finally, using the McWhirter criterion, we confirmed that the considered early stage plasma is in LTE.

Funding. Instytut Maszyn PrzepŁ, ywowych im. Roberta Szewalskiego Polskiej Akademii Nauk (IMP PAN O3T1Z3).

Disclosures. The authors declare no conflicts of interest.

REFERENCES

1. L. Radziemski and D. Cremers, "A brief history of laser-induced breakdown spectroscopy: from the concept of atoms to LIBS 2012," Spectrochim. Acta B Atom. Spectros. **87**, 3–10 (2013).
2. S. K. Hussain Shah, J. Iqbal, P. Ahmad, M. U. Khandaker, S. Haq, and M. Naeem, "Laser induced breakdown spectroscopy methods and applications: a comprehensive review," Radiat. Phys. Chem. **170**, 108666 (2020).
3. D. W. Hahn and N. Omenetto, "Laser-induced breakdown spectroscopy (LIBS), part I: review of basic diagnostics and plasma—particle interactions: still-challenging issues within the analytical plasma community," Appl. Spectrosc. **64**, 335A–336A (2010).
4. R. Noll, C. Fricke-Begemann, S. Connemann, C. Meinhardt, and V. Sturm, "LIBS analyses for industrial applications—an overview of developments from 2014 to 2018," J. Anal. At. Spectrom. **33**, 945–956 (2018).
5. N. L. LaHaye, S. S. Harilal, P. K. Diwakar, and A. Hassanein, "The effect of laser pulse duration on ICP-MS signal intensity, elemental

fractionation, and detection limits in fs-LA-ICP-MS," J. Anal. At. Spectrom. **28**, 1781–1787 (2013).
6. D. Wu, L. Sun, J. Liu, X. Yu, R. Hai, C. Feng, Z. Wang, and H. Ding, "Dynamics of prompt electrons, ions, and neutrals of nanosecond laser ablation of tungsten investigated using optical emission," Phys. Plasmas **26**, 013303 (2019).
7. J. Hermann, E. Axente, V. Craciun, A. Taleb, and F. Pelascini, "Evaluation of pressure in a plasma produced by laser ablation of steel," Spectrochim. Acta B Atom. Spectros. **143**, 63–70 (2018).
8. J. R. Freeman, S. S. Harilal, P. K. Diwakar, B. Verhoff, and A. Hassanein, "Comparison of optical emission from nanosecond and femtosecond laser produced plasma in atmosphere and vacuum conditions," Spectrochim. Acta B Atom. Spectros. **87**, 43–50 (2013).
9. Y. Qiu, J. Wu, Z. Zhang, T. Liu, F. Xue, Y. Hang, Y. Wu, H. Yu, and X. Li, "Comparisons of laser-produced plasma in atmosphere between fiber-delivery and direct-focusing laser pulse," Spectrochim. Acta B Atom. Spectros. **155**, 12–23 (2019).
10. I. Y. Elnasharty, "Study on the influence of laser pulse duration in the long nanosecond regime on the laser induced plasma spectroscopy," Spectrochim. Acta B Atom. Spectros. **124**, 1–15 (2016).
11. T. U. Rahman, Z. U. Rehman, S. Ullah, H. Qayyum, B. Shafique, R. Ali, U. Liaqat, A. H. Dogar, and A. Qayyum, "Laser-induced plasma-assisted ablation (LIPAA) of glass: effects of the laser fluence on plasma parameters and crater morphology," Opt. Laser Technol. **120**, 105768 (2019).
12. V. K. Unnikrishnan, K. Alti, V. B. Kartha, C. Santhosh, G. P. Gupta, and B. M. Suri, "Measurements of plasma temperature and electron density in laser-induced copper plasma by time-resolved spectroscopy of neutral atom and ion emissions," Pramana **74**, 983–993 (2010).
13. M. Skočić, D. Dojić, and S. Bukvić, "Formation of double-layer in the early stage of nanosecond laser ablation," J. Quant. Spectrosc. Radiat. Transfer **227**, 57–62 (2019).
14. A. De Giacomo, R. Gaudiuso, M. Dell'Aglio, and A. Santagata, "The role of continuum radiation in laser induced plasma spectroscopy," Spectrochim. Acta B Atom. Spectros. **65**, 385–394 (2010).
15. S. S. Harilal, C. V. Bindhu, R. C. Issac, V. P. N. Nampoori, and C. P. G. Vallabhan, "Electron density and temperature measurements in a laser produced carbon plasma," J. Appl. Phys. **82**, 2140–2146 (1997).
16. H. Shakeel, S. Arshad, S. U. Haq, and A. Nadeem, "Electron temperature and density measurements of laser induced germanium plasma," Phys. Plasmas **23**, 053504 (2016).
17. A. Palya, O. A. Ranjbar, Z. Lin, and A. N. Volkov, "Kinetic simulations of laser-induced plume expansion into a background gas under conditions of spatial confinement," Int. J. Heat Mass Transfer **132**, 1029–1052 (2019).
18. H. Chang, X. Jin, and W. Zhou, "Experimental investigation of plume expansion dynamics of nanosecond laser ablated Al with small incident angle," Optik **125**, 2923–2926 (2014).
19. H. Zhang, Y. Wu, H. Sun, F. Yang, M. Rong, and F. Jiang, "Investigations of laser-induced plasma in air by Thomson and Rayleigh scattering," Spectrochim. Acta B Atom. Spectros. **157**, 6–11 (2019).
20. D. Bauerle, *Laser Processing and Chemistry*, 3rd ed. (Springer, 2000).
21. S. S. Harilal, C. V. Bindhu, M. S. Tillack, F. Najmabadi, and A. C. Gaeris, "Internal structure and expansion dynamics of laser ablation plumes into ambient gases," J. Appl. Phys. **93**, 2380–2388 (2003).
22. Y. Zhou, B. Wu, S. Tao, A. Forsman, and Y. Gao, "Physical mechanism of silicon ablation with long nanosecond laser pulses at 1064nm through time-resolved observation," Appl. Surf. Sci. **257**, 2886–2890 (2011).
23. Z. Zhang, F. Geng, J. Huang, X. Y. Zhou, S. Q. Feng, X. L. Cheng, X. D. Jiang, W. D. Wu, W. G. Zheng, and Y. J. Tang, "Spectral and temporal characteristics of air-plasma continuum generated by nanosecond laser at 355 nm," Opt. Laser Technol. **56**, 358–361 (2014).
24. H. R. Griem, *Principle of Plasma Spectroscopy*, 1st ed. (Cambridge University, 1997).
25. P. Yeates, "Biberman 'free–bound' continuum correction factor approximation for line-to-continuum temperature diagnostic of aluminium laser plasma," J. Phys. B **44**, 075002 (2011).
26. B. Y. Man, Q. L. Dong, A. H. Liu, X. Q. Wei, Q. G. Zhang, J. L. He, and X. T. Wang, "Line-broadening analysis of plasma emission produced by laser ablation of metal Cu," J. Opt. A **6**, 17–21 (2003).
27. A. Safi, S. H. Tavassoli, G. Cristoforetti, S. Legnaioli, V. Palleschi, F. Rezaei, and E. Tognoni, "Determination of excitation temperature in laser-induced plasmas using columnar density Saha–Boltzmann plot," J. Adv. Res. **18**, 1–7 (2019).
28. M. Skočić and S. Bukvić, "Laser induced plasma expansion and existence of local thermodynamic equilibrium," Spectrochim. Acta B Atom. Spectros. **125**, 103–110 (2016).
29. G. Cristoforetti, E. Tognoni, and L. A. Gizzi, "Thermodynamic equilibrium states in laser-induced plasmas: from the general case to laser-induced breakdown spectroscopy plasmas," Spectrochim. Acta B Atom. Spectros. **90**, 1–22 (2013).
30. H. J. Kunze, *Introduction to Plasma Spectroscopy*, 1st ed. (Springer, 2009).
31. S. Zhang, X. Wang, M. He, Y. Jiang, B. Zhang, W. Hang, and B. Huang, "Laser-induced plasma temperature," Spectrochim. Acta B Atom. Spectros. **97**, 13–33 (2014).
32. M. Burger, D. Pantić, Z. Nikolić, and S. Djeniže, "Shielding effects in the laser-generated copper plasma under reduced pressures of He atmosphere," J. Quant. Spectrosc. Radiat. Transfer **170**, 19–27 (2016).
33. J. Davis, K. G. Whitney, and J. P. Apruzese, "The importance of photoexcitation to the ionization dynamics of laser-produced carbon plasmas," J. Quant. Spectrosc. Radiat. Transfer **20**, 353–370 (1978).
34. D. Diaz and D. W. Hahn, "Plasma chemistry produced during laser ablation of graphite in air, argon, helium and nitrogen," Spectrochim. Acta B Atom. Spectros. **166**, 105800 (2020).
35. Y. Ushirozawa and K. Wagatsuma, "Excitation mechanisms of copper ionic and atomic lines emitted from a low-pressure argon laser-induced plasma," Spectrosc. Lett. **38**, 539–555 (2005).
36. S. S. Harilal, N. Farid, J. R. Freeman, P. K. Diwakar, N. L. LaHaye, and A. Hassanein, "Background gas collisional effects on expanding fs and ns laser ablation plumes," Appl. Phys. A **117**, 319–326 (2014).
37. H. R. Griem, *Spectral Line Broadening by Plasmas*, 1st ed. (Academic, 1974).
38. M. Burger, M. Skočić, Z. Nikolić, S. Bukvić, and S. Djeniže, "Broadening of the resonance Cu I lines in the laser-induced copper spectrum," J. Quant. Spectrosc. Radiat. Transfer **133**, 589–595 (2014).
39. N. Konjević, M. Ivković, and S. Jovićević, "Spectroscopic diagnostics of laser-induced plasmas," Spectrochim. Acta B Atom. Spectros. **65**, 593–602 (2010).
40. N. Konjević, "Plasma broadening and shifting of non-hydrogenic spectral lines: present status and applications," Phys. Rep. **316**, 339–401 (1999).
41. M. A. Gigosos and V. Cardeñoso, "New plasma diagnosis tables of hydrogen Stark broadening including ion dynamics," J. Phys. B **29**, 4795–4838 (1996).
42. K. Zehra, S. Bashir, S. A. Hassan, A. Hayat, and M. Akram, "Spectroscopic and morphological investigation of laser ablated silicon at various laser fluences," Optik **164**, 186–200 (2018).
43. M. Hanif, M. Salik, and M. A. Baig, "Quantitative studies of copper plasma using laser induced breakdown spectroscopy," Opt. Lasers Eng. **49**, 1456–1461 (2011).
44. J. He and Q. Zhang, "A simple method for laser-induced plasma diagnostics under condition of optically thin," Mod. Phys. Lett. B **30**, 1650197 (2016).
45. N. Konjević, A. Lesage, J. R. Fuhr, and W. L. Wiese, "Experimental Stark widths and shifts for spectral lines of neutral and ionized atoms (a critical review of selected data for the period 1989 through 2000)," J. Phys. Chem. Ref. Data **31**, 819–927 (2002).
46. R. W. P. McWhirter, *Plasma Diagnostic Techniques: Spectral intensities*, R. H. Huddlestone and S. L. Leonard, eds. (Academic, 1965), pp. 201–264.
47. N. Singh, A. Goyal, and S. Chaurasia, "Characterization of hot dense plasma with plasma parameters," Radiat. Phys. Chem. **146**, 105–114 (2018).
48. Y. Zhang, Z. Zhao, T. Xu, G. Niu, Y. Liu, and Y. Duan, "Characterization of local thermodynamic equilibrium in a laser-induced aluminum alloy plasma," Appl. Opt. **55**, 2741–2747 (2016).